Chapter 23
On Transverse Shear Strains Treatment in Nine-Node Shell Element MITC9i

Krzysztof Wiśniewski and Ewa Turska

Abstract This chapter concerns a nine-node quadrilateral shell element MITC9i based on the Reissner-Mindlin kinematics and Green strain, which is developed from the potential energy functional extended to include drilling rotations Wisniewski and Turska (2018).
We test an alternative treatment of the transverse shear strains in this element motivated by results of the *Curved cantilever* test of Wisniewski and Turska (2019). In the original MITC9i element, these strains are sampled using the 2×3 and 3×2-point schemes, with all sampling points in the element's interior. In the tested MITC9i2 element, analogous schemes are used, but 8 of the sampling points are located at the element's boundaries. Both elements use the same MITCi transformations.
Several numerical examples are provided to characterize the performance of MITC9i2 compared with two other nine-node elements MITC9i and 9-EAS11.

Key words: 9-node shell element MITC9i · Two-level approximations of strains · Transverse shear strains · Corrected shape functions · Patch tests · Robustness to shape distortions

23.1 Introduction

The basic (unmodified) nine-node element is excessively stiff and sensitive to shape distortion, therefore, several techniques have been proposed to mitigate these problems.

Krzysztof Wiśniewski
Institute of Fundamental Technological Research, Polish Academy of Sciences, Warsaw, Poland
e-mail: kwisn@ippt.pan.pl

Ewa Turska
Polish Japanese Academy of Information Technology, Warsaw, Poland
e-mail: eturska@pjwstk.edu.pl

H. Altenbach et al. (eds.), *Analysis of Shells, Plates, and Beams*, Advanced Structured Materials 134,
https://doi.org/10.1007/978-3-030-47491-1_23

1. One of the first methods was Selective Reduced Integration (SRI) (Pawsey and Clough, 1971), which uses different integration schemes for various parts of the strain energy. The strain components are computed at different points, which restricts the range of application of this method.
2. To overcome this problem, two-level approximations of strains were proposed in which strain components are sampled at selected points and interpolated over the element's domain to allow a uniform 3×3 Gauss integration. This method is know as either the *Assumed Strain* (AS) method (Huang and Hinton, 1984, 1986; Huang, 1989) or the *Mixed Interpolation of Tensorial Components* (MITC) method (Bathe and Dvorkin, 1986; Bucalem and Bathe, 1993). When applied to transverse shear strains, also as the *Assumed Natural Strain* (ANS) method, e.g. for the nine-node elements in Jang and Pinsky (1987); Bischoff and Ramm (1997).

In this chapter we consider our nine-node shell element designated MITC9i of Wisniewski and Turska (2018). The original nine-node MITC9 element has good accuracy but does not pass the five-element patch test of Robinson and Blackham (1979) even for regular meshes, i.e. with straight edges and central positions of side nodes and the interior node. In Wisniewski and Panasz (2013), we proposed improved transformations, which resolved this problem for membrane strains. An extension to bending/twisting and transverse shear strains was given in Wisniewski and Turska (2018).

Another problem concerning nine-node elements is to pass the patch test for the mesh distorted by shifts of mid-side and central nodes, see Sect. 23.4.1 for details. Instrumental in solving this problem are the so-called *Corrected Shape Functions* (CSF) of Celia and Gray (1984), where they are tested for an eight-node (serendipity) element for the Laplace equation (heat conduction) and the 4×4 integration rule. We extend them to shells in Wisniewski and Turska (2018), so the MITC9i shell element passes this test for parallel shifts of the midside nodes and arbitrary shifts of the central node. The CSF were shown to be beneficial for several other types of nine-node elements in Panasz et al (2013); Wisniewski and Turska (2019).

In this chapter the focus is on the transverse shear strains in the MITC9i element. This is motivated by the *Curved cantilever* test of Wisniewski and Turska (2019) Sect. 5.2, in which the EAS11/DISP/ANS shell element (our implementation) had performed slightly better than MITC9i. We attribute this to the treatment of transverse shear strains and, for this reason, now, we implement the ANS method in our MITC9i shell element and check how this affects its overall performance - the tested element is designated MITC9i2. Note that for the transverse shear strains, the ANS method of Jang and Pinsky (1987) is identical to the proposed earlier AS method of Huang and Hinton (1986), see the comment in Jang and Pinsky (1987) p. 2390.

23.2 Shell Equations with Drilling Rotation

23.2.1 Two-field Functional

In the present work, we use a two-field extended shell functional depending on displacements and three-parameter rotations,

$$F_2(\boldsymbol{\chi}, \mathbf{Q}_0) \doteq \int_B \mathcal{W}(\mathbf{C})\,\mathrm{d}V + F_{\text{ext}} + F_{\text{drill}}(\boldsymbol{\chi}, \mathbf{Q}_0), \tag{23.1}$$

where $\boldsymbol{\chi}$ is the deformation function and $\mathbf{Q}_0 \in SO(3)$ is the rotation tensor. The strain energy density $\mathcal{W}$ depends on the right Cauchy-Green deformation tensor $\mathbf{C} \doteq \mathbf{F}^T\mathbf{F}$, where $\mathbf{F} \doteq \nabla\boldsymbol{\chi}$ is the deformation gradient. F_{ext} is the potential of external loads. The last component in Eq. (23.1) is added to incorporate the drilling rotation using the penalty method,

$$F_{\text{drill}} \doteq \frac{1}{2}\int_M \gamma c^2\,\mathrm{d}A, \qquad c \doteq \frac{1}{2}\left[(\mathbf{F}_0\mathbf{t}_2)\cdot(\mathbf{Q}_0\mathbf{t}_1) - (\mathbf{F}_0\mathbf{t}_1)\cdot(\mathbf{Q}_0\mathbf{t}_2)\right], \tag{23.2}$$

where c is the (1,2) component of the Rotation Constraint (RC) equation

$$\operatorname{skew}(\mathbf{Q}_0^T\mathbf{F}_0) = \mathbf{0}$$

and $\gamma \in (0,\infty)$ is the regularization parameter. For the second-order shell kinematics based on the RC equation see Wisniewski and Turska (2002). Note that $\mathbf{F}_0$ and $\mathbf{Q}_0$ are associated with the reference (middle) shell surface at the initial configuration, and $\mathbf{t}_1$ and $\mathbf{t}_2$ are the tangent vectors of the local Cartesian basis on this surface.

23.2.2 Reissner-Mindlin Kinematics

The initial configuration of the shell is parameterized by the natural coordinates $\xi,\eta \in [-1,+1]$ on the reference (middle) surface, and the normal coordinate $z \in [-h/2,+h/2]$, where h is the initial shell thickness, see Fig. 23.1. For the deformed configuration, we use the Reissner-Mindlin kinematical assumptions,

$$\mathbf{x}(\xi,\eta,z) = \mathbf{x}_0(\xi,\eta) + z\,\mathbf{Q}_0(\xi,\eta)\mathbf{t}_3(\xi,\eta), \tag{23.3}$$

where $\mathbf{x}$ is a position vector at an arbitrary z and $\mathbf{x}_0$ at $z = 0$. Besides, $\mathbf{t}_3$ is the unit normal vector in the initial configuration. The rotation tensor $\mathbf{Q}_0$ is parameterized by the canonical rotation vector $\boldsymbol{\psi}$,

$$\mathbf{Q}_0(\boldsymbol{\psi}) \doteq \mathbf{I} + \frac{\sin\omega}{\omega}\tilde{\boldsymbol{\psi}} + \frac{1-\cos\omega}{\omega^2}\tilde{\boldsymbol{\psi}}^2, \tag{23.4}$$

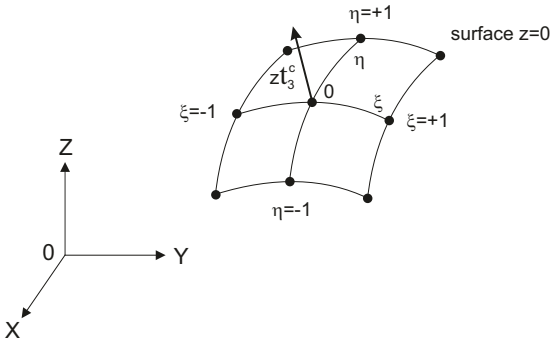

Fig. 23.1 The reference surface ($z = 0$) of nine-node shell element.

where $\omega = \|\boldsymbol{\psi}\| = \sqrt{\boldsymbol{\psi}\cdot\boldsymbol{\psi}} \geq 0$ and $\tilde{\boldsymbol{\psi}} \doteq \boldsymbol{\psi}\times\mathbf{I}$. This form of $\mathbf{Q}_0$ is used only within a load step; in the rotation update scheme devised to handle large rotations it is combined with quaternions.

The deformation function $\boldsymbol{\chi}: \mathbf{x} = \boldsymbol{\chi}(\mathbf{X})$maps the initial (non-deformed) configuration of a shell onto the current (deformed) one. Let us write the deformation gradient as follows:

$$\mathbf{F} \doteq \frac{\partial \mathbf{x}}{\partial \mathbf{X}} = \frac{\partial \mathbf{x}}{\partial \boldsymbol{\xi}}\mathbf{J}^{-1}, \tag{23.5}$$

where $\boldsymbol{\xi} \doteq \{\xi,\eta,z\}$ and the Jacobian matrix $\mathbf{J} \doteq \partial\mathbf{X}/\partial\boldsymbol{\xi}$. The right Cauchy-Green deformation tensor is $\mathbf{C} \doteq \mathbf{F}^T\mathbf{F}$ and the Green strain is defined as $\mathbf{E} \doteq \frac{1}{2}(\mathbf{C}-\mathbf{C}_0)$, where $\mathbf{C}_0 \doteq \mathbf{C}|_{\mathbf{x}=\mathbf{X}} = \mathbf{I}$. The Green strain can be linearized in z,

$$\mathbf{E}(z) \approx \mathbf{E}_0 + z\,\mathbf{E}_1, \tag{23.6}$$

where the *0th order* strain $\mathbf{E}_0$ includes the membrane components $\boldsymbol{\varepsilon}$ and the transverse shear components $\boldsymbol{\gamma}/2$ while the *1st order* strain $\mathbf{E}_1$ includes the bending/twisting components $\boldsymbol{\kappa}$. The transverse shear part of $\mathbf{E}_1$ is typically neglected, i.e. $\kappa_{\alpha 3} \approx 0$ ($\alpha = 1,2$). By Eq. (23.3), the normal shell strains ε_{33} and κ_{33} are equal to zero and in the current work are recovered from the plane stress condition. For details on formulation of our shell finite elements (see Wisniewski, 2010; Wisniewski et al, 2010).

23.3 Characteristics of MITC9i2 Shell Element

A formulation of the MITC9i2 element is similar to that of the MITC9i element described in Wisniewski and Turska (2019). It also uses the Corrected Shape Functions (CSF), which are an important ingredient of the element's formulation, enabling passing some of the patch tests for distorted elements. Essential in this chapter is a treatment of the transverse shear strains, which differs the tested MITC9i2 from MITC9i.

23.3.1 Corrected Shape Functions for Nine-node Shell Element

The standard isoparametric shape functions for a nine-node element are derived for the side nodes 5,6,7 and 8 located exactly between the corner nodes and the central node 9 exactly at the element's center. When these nodes are shifted from the middle positions then the parametric lines (ξ=const. or η=const.) are distorted, see e.g. Figs. 13a and 20 in Panasz et al (2013), and the element's accuracy deteriorates.

To alleviate this problem, the Corrected Shape Functions (CSF) were proposed in Celia and Gray (1984) with six shifts parameters $\alpha,\beta,\gamma,\epsilon,\theta,\kappa \in [-1,+1]$, see Fig. 23.2b. In that paper they are tested for an eight-node (serendipity) element for the Laplace equation (heat conduction) and the 4×4 integration rule. We extended the application range of these functions by considering the nine-node element for plane elasticity with the 3×3 integration, Wisniewski and Panasz (2013); Panasz et al (2013).

The CSF for the nine-node element are defined in two steps. First, the CSF of the 8-node element are defined, which account for shifts of the midside nodes and, next, the basis function for the central node 9 is added hierarchically to them as follows:

$$\begin{aligned} N_i(\xi,\eta) &= \bar{N}_i(\xi,\eta) - \bar{N}_i(\theta,\kappa)N_9(\xi,\eta), \qquad i = 1,\ldots,8, \\ N_9 &\doteq \frac{(\xi^2-1)(\eta^2-1)}{(\theta^2-1)(\kappa^2-1)}, \end{aligned} \tag{23.7}$$

where $\bar{N}_i(\theta,\kappa) \doteq \bar{N}_i(\xi=\theta,\eta=\kappa)$, see Celia and Gray (1984), Eq. (20). When the shift parameters are equal to zero then the CSF of Eq. (23.7) reduce to the standard isoparametric shape functions.

The shift parameters are computed as proportional to the distance in the physical space, and to determine them, we solve 4 equations with 1 unknown for the midside nodes and 2 equations with 2 unknowns for the central node. These equations are nonlinear but are solved only once, so the time overhead is insignificant.

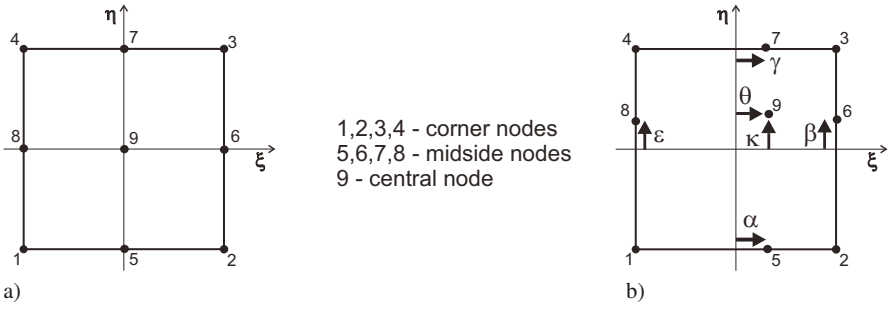

Fig. 23.2. Nine-node element: a) Numbering and naming of nodes, b) Shift parameters for Corrected Shape Functions (CSF).

In Wisniewski and Turska (2018), several extensions of this method of calculating the shift parameters are presented, to enable the use of the CSF to nine-node shell elements located in 3D space; we refer the reader interested in details to this paper. We implemented these extensions in all our nine-node elements. The CSF enable to pass some of the patch tests for elements distorted by shifts of midside and central nodes, see Sect. 23.4.1.

23.3.2 Alternative Version of MITCi Method for Transverse Shear Strains

We consider the MITC (*Mixed Interpolation of Tensorial Components*) method, which is also called the ANS (*Assumed Natural Strain*) method in the literature. The "MITCi" stands for the *improved* MITC method proposed for 2D elements in Wisniewski and Panasz (2013), and based on modified transformations enabling passing the patch test for a regular mesh. They were directly used to the membrane strains $\boldsymbol{\varepsilon}$ of the shell element MITC9i in Wisniewski and Turska (2018); analogous transformations for the bending/twisting strains $\boldsymbol{\kappa}$ and the transverse shear strains $\boldsymbol{\gamma}$ of this element were given and tested therein.

The transverse shear strains $\boldsymbol{\gamma}$ are treated in the MITC9i element using the two-level approximations and the following transformation steps:

1. The representations in the reference Cartesian basis are transformed to the co-basis at the element center to obtain the COVc components,

$$\boldsymbol{\gamma}_{\xi} = \mathbf{j}_c^T \boldsymbol{\gamma}^{\mathrm{ref}}, \tag{23.8}$$

   where $\mathbf{j} \doteq [J_{\alpha\beta}]$ $(\alpha,\beta = 1,2)$ is a 2×2 sub-matrix of $\mathbf{J}$, and the subscript c designates its value at the element center. Note that the components yielded by $\mathbf{j}_c$ instead of $\mathbf{j}$ are not exactly the covariant components; that's why we designate them by "COVc".
2. The two-level approximations of the COVc components are performed,

$$\boldsymbol{\gamma}_{\xi} \overset{\mathrm{MITC}}{\longrightarrow} \widetilde{\boldsymbol{\gamma}}_{\xi}, \tag{23.9}$$

   which involves sampling and interpolation, which are described in detail below.
3. The approximated COVc components $\widetilde{\boldsymbol{\gamma}}_{\xi}$ are transformed back from the co-basis at the element center to the reference Cartesian basis,

$$\widetilde{\boldsymbol{\gamma}}^{\mathrm{ref}} = \mathbf{j}_c^{-T} \widetilde{\boldsymbol{\gamma}}_{\xi}. \tag{23.10}$$

The transformations of the first and the third steps are reciprocal and without the second step we would obtain $\widetilde{\boldsymbol{\gamma}}^{\mathrm{ref}} = \boldsymbol{\gamma}^{\mathrm{ref}}$. Note that the elemental basis can serve as the reference Cartesian basis.

Let us consider the second step of Eq. (23.9), which involves sampling and interpolation, and describe it separately for MITC9i and for MITC9i2. We consider only $\gamma_{31\xi}$; an analogous reasoning applies to $\gamma_{32\xi}$. In both elements, $a = \sqrt{1/3}$.

23.3.2.1 Scheme of MITC9i

A basis of the sampling strategy used in MITC9i is the scheme, which uses the 2×3-point scheme for γ_{31} (see Fig. 23.3a) and the 3×2-point scheme for γ_{32}, totally 12 sampling points. Their position coincides with the integration points for the Selective Reduced Integration (SRI) of strain energy terms of Pawsey and Clough (1971), Table I. They were subsequently used in the MITC element of Bucalem and Bathe (1993) and in the 9-AS element of Panasz and Wisniewski (2008). Note that this sampling does not guarantee continuity of the transverse shear strain components between two adjacent elements.

The transverse shear strains are interpolated as follows:

$$\widetilde{\gamma}_{31\xi}(\xi,\eta) = \sum_i R_i(\xi,\eta)(\gamma_{31\xi})_i, \qquad \widetilde{\gamma}_{32\xi}(\xi,\eta) = \sum_i R_i(\xi,\eta)(\gamma_{32\xi})_i, \tag{23.11}$$

where $i = A,B,C,D,E,F$ is the index of sampling points. The interpolation functions R_i are defined as:

1. for $\gamma_{31\xi}$, the points of Fig. 23.3a are used (2 points in the ξ-direction),

$$\begin{aligned}
R_A(\xi,\eta) &= \tfrac{1}{4}(1-\tfrac{\xi}{a})\left[(\tfrac{\eta}{b})^2-\tfrac{\eta}{b}\right], & R_B(\xi,\eta) &= \tfrac{1}{4}(1+\tfrac{\xi}{a})\left[(\tfrac{\eta}{b})^2-\tfrac{\eta}{b}\right],\\
R_C(\xi,\eta) &= \tfrac{1}{4}(1+\tfrac{\xi}{a})\left[(\tfrac{\eta}{b})^2+\tfrac{\eta}{b}\right], & R_D(\xi,\eta) &= \tfrac{1}{4}(1-\tfrac{\xi}{a})\left[(\tfrac{\eta}{b})^2+\tfrac{\eta}{b}\right],\\
R_E(\xi,\eta) &= \tfrac{1}{2}(1+\tfrac{\xi}{a})\left[1-(\tfrac{\eta}{b})^2\right], & R_F(\xi,\eta) &= \tfrac{1}{2}(1-\tfrac{\xi}{a})\left[1-(\tfrac{\eta}{b})^2\right].
\end{aligned} \tag{23.12}$$

2. for $\gamma_{32\xi}$, analogous points are used (2 points are in the η-direction), and analogous interpolation functions to these of Eq. (23.12) but with ξ and η interchanged.

To reduce the number of evaluations, we proposed a so-called improved sampling strategy for our previous element 9-AS (Panasz and Wisniewski, 2008) and we use it also in MITC9i. The sampling and numerical integration are considered together, which simplifies the code and yields a more efficient implementation.

To explain the method, let us consider $\gamma_{31\xi}$, for which the sampling points and the integration points are shown in Fig. 23.3a. We see that both these types of points are located at the same $\eta \in \{-b,0,+b\}$, where $b = \sqrt{3/5}$. Because, the 3×3 Gauss integration evaluates $\gamma_{31\xi}$ at these values of η, no sampling in the η-direction is needed, and we can sample and interpolate $\gamma_{31\xi}$ only in the ξ-direction,

$$\widetilde{\gamma}_{31\xi}(\xi,\eta) = R_{L1}(\xi)\,\gamma_{31\xi}(-a,\eta) + R_{L2}(\xi)\,\gamma_{31\xi}(+a,\eta), \tag{23.13}$$

where

$$R_{L1}(\xi) = \frac{1}{2}\left(1-\frac{\xi}{a}\right), \qquad R_{L2}(\xi) = \frac{1}{2}\left(1+\frac{\xi}{a}\right), \tag{23.14}$$

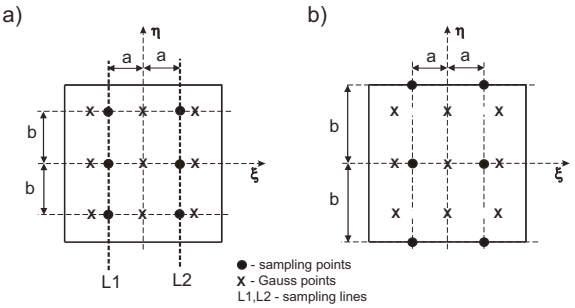

Fig. 23.3 2×3-point sampling schemes for $\gamma_{31\xi}$: a) in MITC9i ($b=\sqrt{3/5}$), b) in MITC9i2 ($b=1$)

The two sampling lines are shown in Fig. 23.3a, where $L1$ is located at $\xi=-a$ and $L2$ at $\xi=a$ ($a=\sqrt{1/3}$).

23.3.2.2 Sampling in MITC9i2

In the tested MITC9i2 element, we use the ANS scheme of Jang and Pinsky (1987); Bischoff and Ramm (1997), which for transverse shear strains is exactly as the scheme proposed earlier within the AS method in Huang and Hinton (1986), see the comment in Jang and Pinsky (1987) p. 2390. It uses the 2×3-point scheme for γ_{31} and the 3×2-point scheme for γ_{32}, but now the value $b=1$ is used, so 8 sampling points are located at element's edges, see Fig. 23.3b. The value of $a=\sqrt{1/3}$ is the same as used in MITC9i. The transverse shear strains are interpolated as in Eq. (23.11) and the interpolation functions R_i are defined as in Eq. (23.12), but now $b=1$ should be used. Note that the improved sampling strategy of Eqs. (23.13)-(23.14), which was used in MITC9i, cannot be used here.

23.4 Numerical Examples

In this section, we present numerical tests of the nine-node shell element MITC9i2, which is a modified version of the MITC9i of Wisniewski and Turska (2018) with an alternative transverse shear part described in Sect. 23.3.2. The formulation of this element and the reference elements are characterized in Table 23.1; other FEs are also used for comparison in examples. All the shell elements are of the Reissner-Mindlin type and have 6 dofs/node; the drilling rotation is incorporated as specified in eqs. (23.1)-(23.2), for more details see Sects. 2 and 5 of Wisniewski and Turska (2018). Note that in all these elements:

1. the *Corrected Shape Functions* (CSF) are implemented in the version extended to shells in Wisniewski and Turska (2018), Sect. 4,
2. the 3×3 Gauss integration is used, which yields a correct rank (6 zero eigenvalues) of the elements.

Table 23.1
Formulation of nine-node shell elements with drilling rotation.

Element	Strains membrane $\boldsymbol{\varepsilon}$	bending $\boldsymbol{\kappa}$	transverse shear $\boldsymbol{\gamma}$
Tested element			
MITC9i2	MITCi	MITCi	ANS of Jang and Pinsky (1987)
Reference elements			
MITC9i Wisniewski and Turska (2018)	MITCi	MITCi	MITCi
9-EAS11[a] Bischoff and Ramm (1997), Wisniewski and Turska (2019)	EAS11	DISP[b]	ANS of Jang and Pinsky (1987)

[a] In Wisniewski and Turska (2019), this element is designated 9-EAS11/DISP/ANS.
[b] DISP - strain is not modified.

These elements were derived by ourselves using the automatic differentiation program AceGen of Korelc (2002), and were tested within the finite element program FEAP of R.L. Taylor (Zienkiewicz and Taylor, 1989); the use of these programs is gratefully acknowledged. Our parallel multithreaded (OMP) version of FEAP is described in Jarzebski et al (2015).

23.4.1 Patch Tests

We run the five-element patch test of Robinson and Blackham (1979), but also for the mesh distorted by shifts of selected mid-side and central nodes marked in Fig. 23.4. The membrane and bending patch tests are performed as described in Macneal and Harder (1985); the transverse shear test is performed for the load case defined for a nine-node plate in Huang and Hinton (1984), see *Shearing case* in Fig. 2b therein.

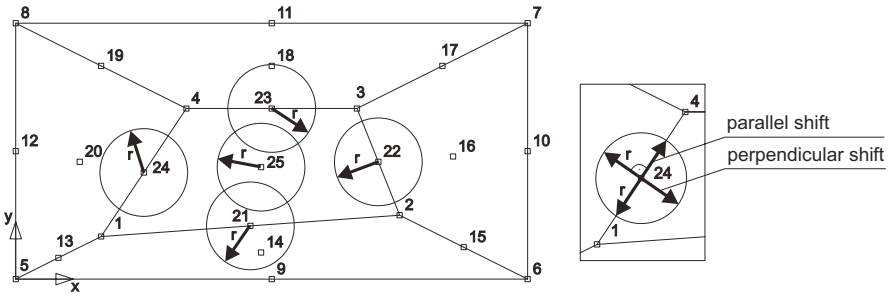

Fig. 23.4. Five-element patch test with shifts of selected nodes (circles not to scale).

Four cases of nodal shifts are considered, see Fig. 23.4: (A) zero shifts (i.e. a regular mesh as in Robinson and Blackham, 1979), (B) arbitrary shifts of node 25, (C) parallel shifts of nodes 21-24, and (D) perpendicular shifts of nodes 21-24, for which edges of the central element become curved. We monitor the level of errors for the analysis with and without the CSF, for more details see Wisniewski and Turska (2018). The conclusions pertaining to performance of the tested MITC9i2 element are as follows:

1. *Membrane patch test.* MITC9i2 performs exactly as MITC9i, because its membrane part is identical. As shown in Wisniewski and Turska (2018), MITC9i passes Case A even for standard shape functions (no CSF), needs the CSF to pass Case B and C, and fails for Case D even with the CSF. The 9-EAS11 element performs better, and passes this test for all cases of nodal shifts using the standard shape functions, see Wisniewski and Turska (2019).
2. *Bending patch test.* For the standard shape functions (no CSF), MITC9i2 passes it for Case A but fails for the other cases. With the CSF, MITC9i2 passes Case B and C; but not D. Recall from Wisniewski and Turska (2019) that the CSF are indispensable also for MITC9i and 9-EAS11, as they enable passing Case B and C, though not D.
3. *Transverse shear patch test.* MITC9i2 passes it for all cases of shifts using the standard shape functions, i.e. the CSF in not needed.

Concluding, we see that MITC9i2 performs similarly to MITC9i, though the errors for the bending patch test and Case D, which is failed, are one order smaller than for MITC9i and the same as for 9-EAS11.

23.4.2 Curved Cantilever

The curved cantilever is fixed at one end and loaded by a moment M_z at the other, see Fig. 23.5. The data is as follows: $E = 2 \times 10^5$, $\nu = 0$, width $b = 0.025$ and radius of curvature $R = 0.1$. The FE mesh consists of 6 nine-node elements, which have either regular (Fig. 23.5a) or distorted shape (Fig. 23.5b); a definition of distortions is given in Koschnick et al (2005) p. 245. For the distorted mesh, this test is very

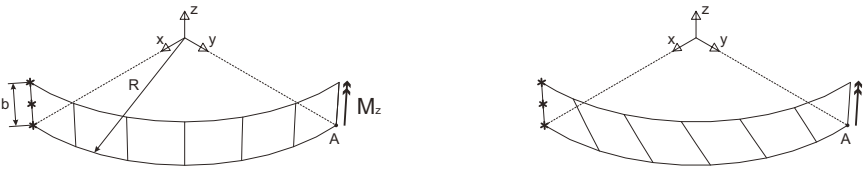

a) b)

Fig. 23.5. Curved cantilever and two meshes: (a) regular and (b) distorted.

demanding. The side and central nodes of elements are not shifted so the CSF do not affect this test.

In Wisniewski and Turska (2019), Sect. 5.2, we established that the shell element 9-EAS11/DISP/ANS (designated 9-EAS11 in the current chapter) performs slightly better than the MITC9i shell element in this test (when the RBF is not used); now we check how the ANS method applied to transverse shear part affects the performance of MITC9i.

The shell thickness h is varied in the range $[10^{-2}, 10^{-6}]$, and the moment is assumed as $M_z = (R/h)^{-3}$, so the solution of a linear problem should remain constant. The analytical solution for the curved beam subjected to uniform bending is $u_y = M_z R^2/(EI) = 0.024$, where I is the moment of inertia.

The displacement u_y at point A obtained by a linear analysis are shown in Fig. 23.6, where, for the vertical axis, we use either (a) the standard scale or (b) the logscale,

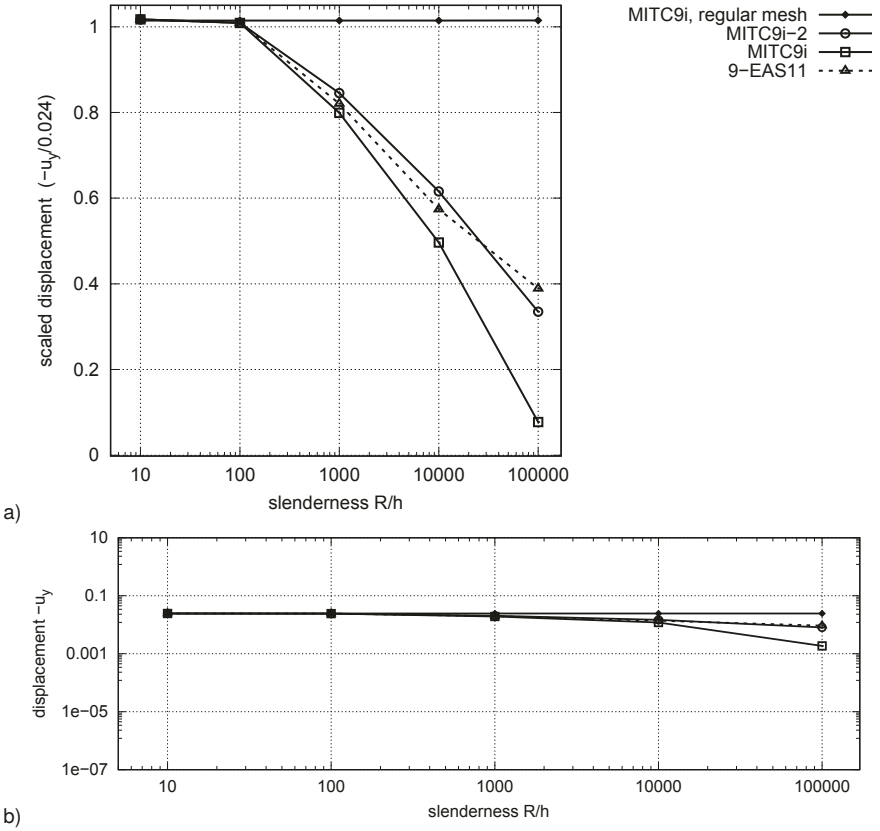

Fig. 23.6. Curved cantilever. Displacement u_y at point A for the distorted mesh and diminishing thickness. $\gamma = G$. a) log-standard scale, b) log-log scale to enable comparisons with Fig. 6 of Koschnick et al (2005).

to enable comparisons with Fig. 6 of Koschnick et al (2005). Additionally, the displacements in Fig. 23.6a are scaled by the analytical solution to quantify the decline of accuracy. We conclude this test as follows:

1. For the regular mesh, the solutions for all tested elements are represented by the horizontal line, which is close to the analytical value. Neither one of the tested elements locks for this mesh despite the curved geometry.
2. For the distorted mesh, all the tested elements lock for $R/h > 100$, and the drop of accuracy for $R/h > 1000$ becomes unacceptable. In the acceptable range, the most accurate is MITC9i2, then 9-EAS11 and MITC9i.
3. Comparing the displacementsu_y of our Fig. 23.6b and Fig. 6 of Koschnick et al (2005) (in both these figures the log-log scale is used, and the displacements are not scaled by the analytical solution), we conclude that the element MITC9i2 performs in this test slightly better than Q2-ANS/EAS.

23.4.3 Homogeneous circular shell

The circular shell is shown in Fig. 23.7. The geometrical data is as follows: radius $R = 1000$ mm, thickness $h = 100$ mm and length $L = 100$ mm, see Wagner and Gruttmann (2019). One straight boundary is clamped while the other straight one is free and loaded by the distributed force $P = 100$ N/mm. Note that $R/h = 10$, i.e. this shell is thick. The stresses are reported at $\theta = \pi/4$, using the user's procedure implemented by ourselves in FEAP to define a direction for the strain/stress output in 2D and 3D.

In the circumferential direction, we use either 20 nine-node shell elements or 40 elements of other types. One element is used in the 0Y direction.

For a similar 2D problem in the X0Z-plane and the plane stress condition applied in the 0Y direction, there exists an analytical stress solution of Timoshenko and Goodier (1951), Sect. 31. The analytical expression (in polar coordinates) for the shear stress is

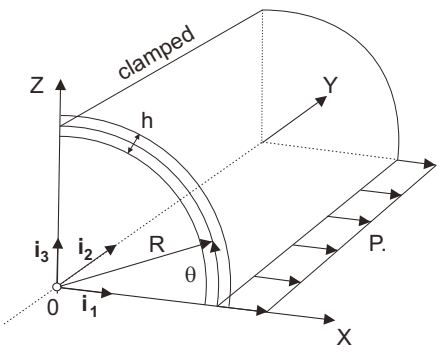

Fig. 23.7 Homogeneous circular shell. Geometry.

$$\sigma_{r\theta}(z,\theta) = -\underline{\frac{1}{d}\left[r + \frac{a^2b^2}{r^3} - \frac{1}{r}(a^2+b^2)\right]}(P\cos\theta), \tag{23.15}$$

where $z \in [-h/2, h/2]$, $r = R + z$, $a = R - h/2$, $b = R + h/2$, and

$$d = a^2 - b^2 + (a^2 + b^2)\log(b/a).$$

Note that an integral over the thickness of the underlined terms is equal to 1, i.e. they characterize a distribution of the shear stress but not its maximum value. The shear stress $\sigma_{r\theta}$ at the cross-section $\theta = \pi/4$ is shown in Fig. 23.8.

The above analytical solution is verified using our 2D 4-node enhanced strain element (EADG4). In the 2D mesh, we use 16 elements in the radial direction (fictive layers of equal thickness) and 40 elements in the circumferential direction. The stress in Eq. (23.15) does not depend on material constants, but in the FE analyses we have to use some values. We assumed $E = 3.8 \cdot 10^5 \mathrm{N/mm^2}$ and $\nu = 0.3$, but for other values, the obtained stress is the same. The shear stress at $\theta = \pi/4$ is shown in Fig. 23.8, and it perfectly matches the analytical $\sigma_{r\theta}$. Both stresses are slightly non-symmetric w.r.t. $z = 0$ due to the curved geometry.

Regarding the Reissner-Mindlin shell elements, the stress resultants are available as a standard in this class of elements, while stresses must be additionally computed. When the shell is curved, we have to specify the orientation vector in an input, and use the shell director to define a basis for the stress resultants' output. In the current example, we use the orientation vector tangent to the reference surface in the X0Z-plane. Having the transverse shear stress resultant N^{31}, we compute a distribution of the transverse shear stress S^{13} and its maximum as follows:

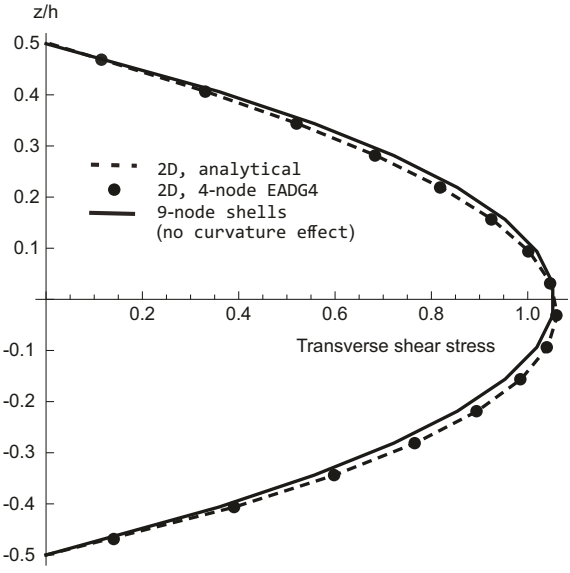

Fig. 23.8 Homogeneous circular shell. Distribution of transverse shear stress at $\theta = \pi/4$.

$$S^{31}(z) = \frac{3}{2h}\left[1 - 2\left(\frac{z}{h}\right)^2\right] N^{31}, \qquad \max S^{31} = S^{31}(z=0). \tag{23.16}$$

This standard formula does not account for the shell curvature, so it is symmetric w.r.t. $z = 0$, see Fig. 23.8. The maximum values for the two versions of the MITC9i shell element are given in Table 23.2.

Table 23.2
Homogeneous circular shell. Transverse shear stress resultant and transverse shear stress at $\theta = \pi/4$.

Element	Stress resultant N^{31}	Max stress S^{31} by Eq. (23.15)b
MITC9i2	69.955	1.049
MITC9i	70.13	1.052
Ref. $P\cos(\pi/4)$	70.71	-

Remark 23.1. To include the curvature in a simple way, we note that the resultant N^{31} corresponds to the term $(P\cos\theta)$ in Eq. (23.15) and use the underlined terms in that equation as the distribution function. Then the transverse shear is defined as

$$S^{31}(z) = -\frac{1}{d}\left[r + \frac{a^2b^2}{r^3} - \frac{1}{r}(a^2+b^2)\right] N^{31}. \tag{23.17}$$

A difference between the value of N^{31} from Table 23.2 and $P\cos(\pi/4) = 70.71$ causes only a small deviation from the exact non-symmetric distribution yielded by Eq. (23.15). We also see that, compared to the value $P\cos(\pi/4) = 70.71$, the resultant N^{31} for MITC9i is slightly more exact than for MITC9i2.

The displacement components in the 0X and 0Z direction (u, v) at the straight free boundary obtained for several types of FEs are given in Table 23.3. For all tested nine-node elements, the displacements are almost identical, differing at most by the last digit of the v-displacement. Additionally, the solutions obtained using our 4-node

Table 23.3
Homogeneous circular shell. Displacements at the straight free boundary.

Element	u-displacement	v-displacement
Tested nine-node shell elements		
MITC9i2, MITC92, 9-EAS11	2.4843	1.5796
Reference elements		
2D 4-node EADG4	2.4786	1.5779
Solid-shell 8-node, ours as in Klinkel et al (2006)	2.4745	1.5732
Shell 4-node HW47 (Wisniewski and Turska, 2012)	2.4847	1.5784

shell element HW47 of Wisniewski and Turska (2012) and our implementation of the 8-node solid-shell element of Klinkel et al (2006) are provided.

23.4.4 Twisted Beam

The initial geometry of the beam is shown in Fig. 23.9; it is twisted but the initial strain is equal to zero (Macneal and Harder, 1985). The beam is clamped at one end and loaded by the out-of-plane force P_y at the other. The data is as follows: $E = 2.9 \times 10^7$, $\nu = 0.22$, the length $L = 12$, the width $w = 1.1$ and the twist is 90°. We use the 2×12-element mesh of nine-node FEs and a very small shell thickness $h = 0.0032$.

The results of a linear analysis for $P_y = 10^{-6}$ are given in Table 23.4, where the displacement $u_y \times 10^3$ at point A is presented. The results for MITC9i2 are slightly

Table 23.4
Twisted beam. Displacement for linear analysis.

Element	$u_y \times 10^3$
MITC9i2	1.2953
MITC9i	1.2948
9-EAS11	1.2952
9 (unmodified)	0.1176
Beam theory (Belytschko et al, 1989)	1.2940

better than for MITC9i and 9-EAS11; they all are a little above the beam theory value. These results are for the regularization parameter for the drilling RC $\gamma = G/1000$; we tested also $\gamma = G$, and the difference was negligible. For this very thin shell, a solution for the unmodified element 9 is very locked (10 times too small), while application of such techniques as the MITC and the EAS is clearly beneficial.

The non-linear load-deflection curves obtained by the arc-length method are shown in Figs. 23.10 and 23.11, where the displacement u_z and u_y at point A are shown, respectively. The initial $\Delta P_y = 10^{-4}$ and the regularization parameter for the drilling RC $\gamma = G/1000$.

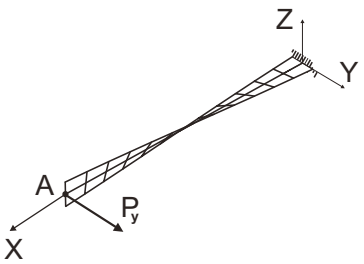

Fig. 23.9 Twisted beam. Geometry and out-of-plane force P_y.

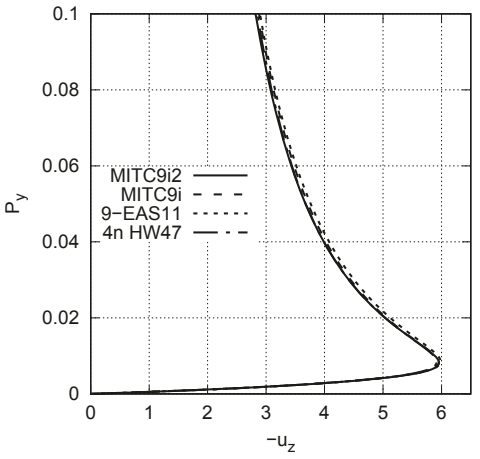

Fig. 23.10 Non-linear twisted beam. Displacement u_z for out-of-plane force.

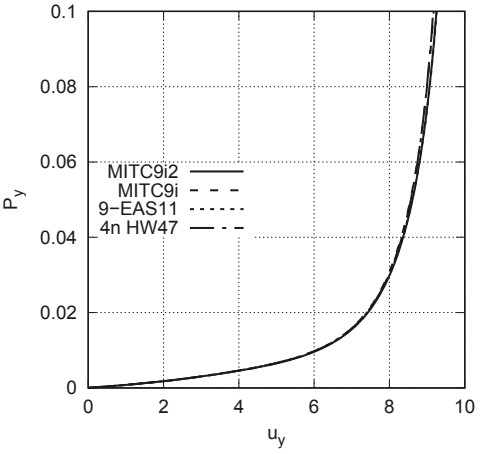

Fig. 23.11 Non-linear twisted beam. Displacement u_y for out-of-plane force.

In Fig. 23.10, which is more indicative, there is almost no difference between the curves for MITC9i2 and MITC9i, and the curve for MITC9i2 nearly coincides with that for the 4-node element HW47 of Wisniewski and Turska (2012). The curve for 9-EAS11 is a little stiffer; it is the curve most to the right after a turning point. As the shell is very thin, similarity of these solutions confirms quality of all these elements.

This example can also be calculated using the load control but the arc-length method enables comparison of the lengths of steps for particular elements. The largest steps are for MITCi2, then for MITC9i and the shortest for 9-EAS11. For 9-EAS11, the initial $0.5\,\Delta P_y$ was used because the element diverged for ΔP_y.

23.4.5 Pinched Hemispherical Shell with Hole

A hemispherical shell with an 18^o hole is loaded by two pairs of equal but opposite external forces P applied along the 0X and 0Y axes, see Fig. 23.12. Because of a double symmetry, a quarter of the hemisphere is modeled. In this test, the shell undergoes an almost in-extensional deformation and, because it is very thin (thickness $h = 0.01$), the membrane locking can manifest itself strongly.

The non-linear solutions were obtained using the Newton method; the inward displacement at point A for the 8×8-element mesh is shown in Fig. 23.13. The differences in solutions are very small; the curves for 9-EAS11 and MITC9i2 fully coincide, while MITC9i is minimally stiffer. On the other hand, we were able to run MITC9i with $\Delta P = 0.2$ for which the other two elements diverged; then $\Delta P = 0.1$ was used. Hence, in this test MITC9i performs better than MITC9i2 and 9-EAS11.

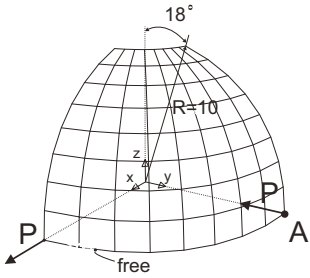

Fig. 23.12 Pinched hemispherical shell with hole. Geometry and load.

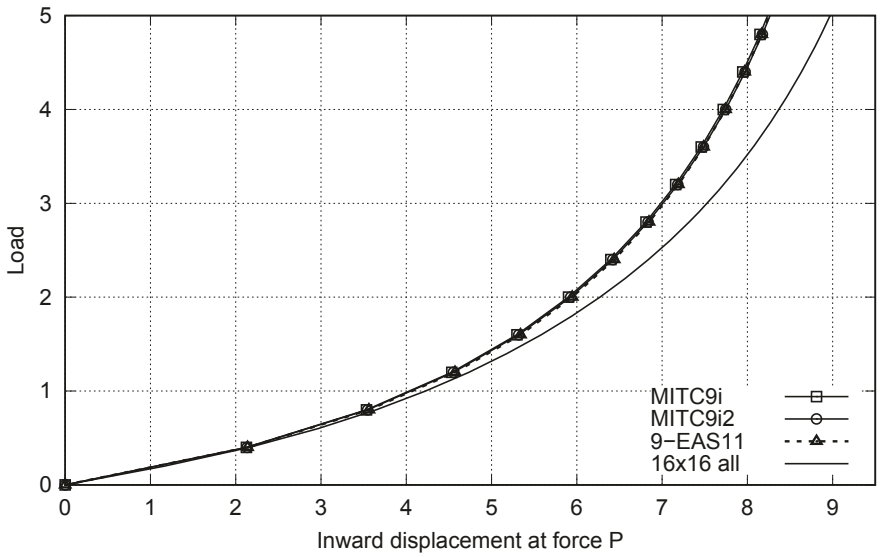

Fig. 23.13. Pinched hemispherical shell with hole. Nonlinear solutions for 8×8 mesh, γ=G/1000.

23.5 Final remarks

We developed a nine-node quadrilateral shell element MITC9i2 with the transverse shear part different than in the MITC9i element. In both these elements, the 2×3 and 3×2-point sampling schemes were used, where in the new element 8 of the sampling points are located at element's boundaries. Five numerical examples are computed and their results can be summarized as follows:

1. *Patch tests:* The membrane and transverse shear patch tests are passed by MITC9i2, with no difference compared to MITC9i. Regarding the bending patch test, MITC9i2 with the CSF passes it for Case B and C of nodal shifts, again there is no difference compared to MITC9i. Similarly to the other nine-node elements, MITC9i2 fails the bending patch test with curved elements' edges (Case D of nodal shifts) though the level of errors is one order lower than for MITC9i.
2. *Curved cantilever:* MITC9i2 is slightly more accurate than 9-EAS11 and MITC9i. Results of this test for the EAS11/DISP/ANS element in Wisniewski and Turska (2019) provided the motivation to modify the transverse shear part of MITC9i, and the new MITC9i2 performs in this test better than MITC9i indeed.
3. *Homogeneous circular shell:* Displacements yielded by MITC9i2 are equally accurate as by the other elements, while the transverse shear stress resultant N^{31} is slightly less accurate than by MITC9i.
4. *Twisted beam:* In the linear tests, MITC9i2 is slightly more accurate than MITC9i and 9-EAS11. In the nonlinear test, MITC9i2 and MITC9i perform almost identically, 9-EAS11 is a little stiffer and requires smaller ΔP_y for the arc-length method than the other elements.
5. *Pinched hemisphere:* In this nonlinear test, MITC9i2 and 9-EAS11 are equally exact, while MITC9i is minimally stiffer, although the differences are very small. On the other hand, MITC9i is more robust, as the Newton method runs with $\Delta P = 0.2$ for which the other two elements diverge.

Generally, these preliminary results demonstrate that the tested element MITC9i2 is of a very good quality. In the linear tests, it is slightly more accurate than MITC9i, but in the nonlinear tests, MITC9i seems to have a larger radius of convergence and to be more robust. Further tests are required before a conclusion is drawn as to whether MITC9i2 should replace our best so far MITC9i element.

References

Bathe KJ, Dvorkin EN (1986) A formulation of general shell elements—the use of mixed interpolation of tensorial components. International Journal for Numerical Methods in Engineering 22(3):697–722

Belytschko T, Wong BL, Stolarski H (1989) Assumed strain stabilization procedure for the 9-node Lagrange shell element. International Journal for Numerical Methods in Engineering 28(2):385–414

Bischoff M, Ramm E (1997) Shear deformable shell elements for large strains and rotations. International Journal for Numerical Methods in Engineering 40(23):4427–4449

Bucalem ML, Bathe KJ (1993) Higher-order MITC general shell elements. International Journal for Numerical Methods in Engineering 36(21):3729–3754

Celia MA, Gray WG (1984) An improved isoparametric transformation for finite element analysis. International Journal for Numerical Methods in Engineering 20(8):1443–1459

Huang HC (1989) Static and Dynamic Analyses of Plates and Shells. Springer, London

Huang HC, Hinton E (1984) A nine node Lagrangian Mindlin plate element with enhanced shear interpolation. Engineering Computations 1(4):369–379

Huang HC, Hinton E (1986) A new nine node degenerated shell element with enhanced membrane and shear interpolation. International Journal for Numerical Methods in Engineering 22(1):73–92

Jang J, Pinsky PM (1987) An assumed covariant strain based 9-node shell element. International Journal for Numerical Methods in Engineering 24(12):2389–2411

Jarzebski P, Wisniewski K, Taylor R (2015) On parallelization of the loop over elements in FEAP. Computational Mechanics 56(1):77–86

Klinkel S, Gruttmann F, Wagner W (2006) A robust non-linear solid shell element based on a mixed variational formulation. Computer Methods in Applied Mechanics and Engineering 195(1):179–201

Korelc J (2002) Multi-language and multi-environment generation of nonlinear finite element codes. Engineering with Computers 18(4):312–327

Koschnick F, Bischoff M, Camprubí N, Bletzinger KU (2005) The discrete strain gap method and membrane locking. Computer Methods in Applied Mechanics and Engineering 194(21):2444–2463

Macneal RH, Harder RL (1985) A proposed standard set of problems to test finite element accuracy. Finite Elements in Analysis and Design 1(1):3–20

Panasz P, Wisniewski K (2008) Nine-node shell elements with 6 dofs/node based on two-level approximations. Part I: Theory and linear tests. Finite Elements in Analysis and Design 44(12):784–796

Panasz P, Wisniewski K, Turska E (2013) Reduction of mesh distortion effects for nine-node elements using corrected shape functions. Finite Elements in Analysis and Design 66:83–95

Pawsey SF, Clough RW (1971) Improved numerical integration of thick shell finite elements. International Journal for Numerical Methods in Engineering 3(4):575–586

Robinson J, Blackham S (1979) An Evaluation of Lower Order Membranes as Contained in MSC/NASTRAN, ASA and PAFEC FEM Systems. Robinson and Associates, Dorset, England

Timoshenko S, Goodier JN (1951) Theory of Elasticity. McGraw-Hill

Wagner W, Gruttmann F (2019) On a simple shell model for thin structures with functionally graded materials. In: Altenbach H, Chróścielewski J, Eremeyev V,

Wiśniewski K (eds) Recent Developments in the Theory of Shells, Springer, Cham, Advanced Structured Materials, vol 110, pp 687–710

Wisniewski K (2010) Finite Rotation Shells - Basic Equations and Finite Elements for Reissner Kinematics. Springer

Wisniewski K, Panasz P (2013) Two improvements in formulation of nine-node element MITC9. International Journal for Numerical Methods in Engineering 93(6):612–634

Wisniewski K, Turska E (2002) Second-order shell kinematics implied by rotation constraint-equation. Journal of Elasticity 67:229–246

Wisniewski K, Turska E (2012) Four-node mixed hu–washizu shell element with drilling rotation. International Journal for Numerical Methods in Engineering 90(4):506–536

Wisniewski K, Turska E (2018) Improved nine-node shell element MITC9i with reduced distortion sensitivity. Computational Mechanics 62:499–523

Wisniewski K, Turska E (2019) On performance of nine-node quadrilateral shell elements 9-EAS11 and MITC9i. In: Altenbach H, Chróścielewski J, Eremeyev V, Wiśniewski K (eds) Recent Developments in the Theory of Shells, Springer, Cham, Advanced Structured Materials, vol 110, pp 710–725

Wisniewski K, Wagner W, Turska E, Gruttmann F (2010) Four-node Hu–Washizu elements based on skew coordinates and contravariant assumed strain. Computers & Structures 88(21):1278–1284

Zienkiewicz OC, Taylor RL (1989) The Finite Element Method, vol I. Basic Formulation and Linear Problems, 4th edn. McGraw-Hill